PHOTONICS Research

Boosting a sub-10 nm nanogap array by plasmon-triggered waveguide resonance

Yu Tian,[1] Hailong Wang,[1] Yijia Geng,[2] Lili Cong,[1] Yu Liu,[2] Weiqing Xu,[1] and Shuping Xu[1,*]

[1]State Key Laboratory of Supramolecular Structure and Materials, Institute of Theoretical Chemistry, College of Chemistry, Jilin University, Changchun 130012, China
[2]State Key Laboratory of Applied Optics, Changchun Institute of Optics, Fine Mechanics and Physics, Chinese Academy of Sciences, Changchun 130033, China
*Corresponding author: xusp@jlu.edu.cn

Received 30 July 2020; revised 29 September 2020; accepted 29 September 2020; posted 1 October 2020 (Doc. ID 404092); published 17 November 2020

Gap-type metallic nanostructures are widely used in catalytic reactions, sensors, and photonics because the hotspot effect on these nanostructures supports giant local electromagnetic field enhancement. To achieve hotspots, researchers devote themselves to reducing gap distances, even to 1 nm. However, current techniques to fabricate such narrow gaps in large areas are still challenging. Herein, a new coupling way to boost the sub-10 nm plasmonic nanogap array is developed, based on the plasmon-triggered optical waveguide resonance via near-field coupling. This effect leads to an amplified local electromagnetic field within the gap regions equivalent to narrower gaps, which is evidenced experimentally by the surface-enhanced Raman scattering intensity of probed molecules located in the gap and the finite-difference time-domain numerical simulation results. This study provides a universal strategy to promote the performance of the existing hotspot configurations without changing their geometries. © 2020 Chinese Laser Press

https://doi.org/10.1364/PRJ.404092

1. INTRODUCTION

Controlling the light at the nanoscale by plasmonic nanostructures to obtain hotspots with giant local electromagnetic (EM) fields has received increasing interest in the past decade because hotspots are beneficial for catalytic reactions [1–3], biochemical sensors [4–6], plasmon-enhanced photoluminescence [7–9], and plasmon-enhanced spectroscopy [10–12]. Programmed nanogaps are considered one of the most feasible hotspot structures. Diverse preparation methods have been explored actively for building gap-type nanostructures. The skillful control of the gap distance can be achieved in various ways. For example, nanoparticle dimers with the bridging molecular rulers can be made by complementary deoxyribonucleic acid chains [13,14] or other linkers [15]. The gap distances can be precisely controlled even to 1 nm. However, these bridging molecules occupy the gap areas, which limits further applications of these hotspots. The physical methods, e.g., electron-beam lithography and focused ion beam and photon lithography [16,17], allow for the highly ordered, nonmolecule-filled gaps, which are also beneficial for surface-enhanced Raman scattering (SERS) detection and bio/chem sensing [18–20]. However, these methods are time-consuming, and it is challenging to manufacture hotspots in large areas.

In order to pursue stronger local EM fields of the gap configurations, ways to manipulate their radiation processes have been extensively explored in light–matter interactions. One of the strategies is to avoid the nonradiative damping of metal materials caused by interband transitions [21,22]. Other attempts start with the field coupling of many resonance modes, e.g., cavity [23,24], waveguide (WG) [25–28], dielectric sphere [29–31], and other optical elements.

In this work, we demonstrate a useful strategy for boosting a large-area gap-type array based on a modified planar optical WG. The localized surface plasmon resonance (LSPR) of a sub-10 nm Ag nanogap array triggers the planar WG mode, which improves the EM field of gap regions 1.8 times, evidenced by the SERS signals of probed molecules located in gap areas. Typically, an attenuated total reflectance (ATR) mode that can trigger a planar WG resonance is preceded by some optical couplers, e.g., prisms [25–28,32,33], or irradiating the WG from the transverse plane. Here, the WG resonance can be excited by the near-field coupling of the nanogap array, which has hardly been reported in previous studies. This strategy extends the application scope of the plasmon–WG combined systems due to the configuration simplification, with no need for other optical couplers. Thus, a distinct physical

mechanism is proposed. The plasmon resonance first launches, and then couples the light to the dielectric WG to resonance. This plasmon/WG coupling improves the local EM field of the gap regions and facilitates plasmonic sensing and imaging with a higher sensitivity.

2. EXPERIMENTAL SECTION

A. Preparation of the WG

The WG structure was prepared on a BK7 glass slide (1.0 cm × 1.3 cm, $n = 1.516$). A 35 nm Ag film was deposited on a cleaned glass slide by thermal evaporation at a speed of 0.18 nm · s^{-1}. After that, a 600 nm SiO_2 WG layer ($n = 1.48$) was fabricated on the Ag film by the inductively coupled plasma chemical vapor deposition (ICPCVD) method.

B. Preparation of the Ag Nanogap Array

An Ag nanogap array was achieved by opposite oblique evaporation of Ag 2 times by using a double-sided through-hole anodic aluminum oxide (AAO) as a mask, as shown in Fig. 1(a). The AAO templates were purchased from Shenzhen Topological Fine Film Technology Co., Ltd. The period, aperture size, and thickness are 125, 100, and 430 nm, respectively, as shown in Fig. 1(b). A polymethyl methacrylate (PMMA) layer covers one side of the AAO structure as a support layer. The AAO mask was stuck tightly to the surface of the WG layer. Then, the slide was soaked in acetone for 15 min 4 times to remove the PMMA. Thus, the AAO mask was successfully transferred to the WG surface.

To prepare the Ag nanogap array, we put the WG slide with the AAO mask on an inclined stage of a thermal evaporation vessel 2 times for metal evaporation [34–36]. The stage tilted 10° relative to the horizontal direction for the first evaporation step, and then we turned the stage to the opposite synclinal direction for the second evaporation. The thermal evaporation worked at a speed of 0.18 nm · s^{-1}. The obtained nanogap is two close semiellipsoids. To achieve a symmetrical nanogap geometry, the evaporation thicknesses were optimized as 30 nm for the first evaporation and 39 nm for the second evaporation, because the pore size of the AAO would be blocked to a certain extent after the first evaporation step. Finally, the AAO, including the extra Ag on the AAO, was removed with sticky tape. The achieved Ag nanogap array was characterized by a scanning electron microscope (SEM, JEOL JSM-6700F) as shown in Fig. 1(c).

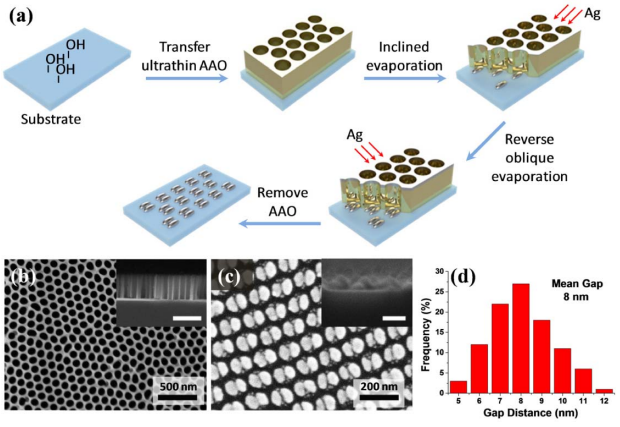

Fig. 1. (a) Preparation process of nanogap arrays; (b) SEM images of the AAO mask. The scale bar of the inset is 500 nm. (c) SEM images of Ag nanogap array. The scale bar of the inset is 100 nm. (d) Statistical results of 100 gap distances.

C. Reflectance Spectra and SERS Measurements

Reflectance spectra and angle-dependent SERS spectra were measured by a self-built angle-dependent surface plasmon resonance-SERS microspectrometer, which can test spectra at different incident and collection angles [37]. This instrument consists of a dual-arm goniometer, an inverted microscope (with a 20× objective lens, NA = 0.35, focal length = 20.5 mm), a CCD imaging camera with a display screen, and a spectrometer (iHR320, Jobin-Yvon Co.) with a CCD (Synapse, Jobin-Yvon Co.). The polarization direction can be adjusted by simply rotating the polarization component, composed of a quarter-wave plate and a polarizer. The wavelength of incident light was 532 nm (450 μW to the sample surface). The time integration for the CCD was 10 s and was done twice.

For the SERS measurements, a drop of a 4-mercaptobenzoic acid (4-MBA) ethanol solution (1.0×10^{-3} mol/L) was dropped onto the surface of the sample, and all measurements were performed after the drop was dried. In order to prevent laser damage to the nanogap array, the weak laser power and high probe concentration were selected.

D. Dark-Field Imaging

The light from a halogen lamp was focused onto the surface of the sample through a 100-fold dark-field lens (NA = 0.8). Dark-field imaging was acquired through a CCD. The integral intensity was figured out by Image J software, and the thresholds were set to 0 to 255 during the statistical process.

E. Numerical Simulations

The simulations were calculated by the 3D finite-difference time-domain (FDTD) numerical method using commercial software (FDTD Solutions, Lumerical Solutions, Inc.). The model parameters were consistent with the experimental parameters. The permittivity of Ag and SiO_2 came from the software's database, and the refractive index of the prism was 1.516. The incident light was a plane wave with a wavelength of 532 nm, and the polarization direction was parallel or perpendicular to the incidence plane. The simulation time was set to 1000 s to ensure the convergence of the results. The incident light scanned from 25° to 65° with an interval of 0.5°, and the electric field distributions were obtained under the resonance angles.

3. RESULTS AND DISCUSSION

A. Structure of the Ag Nanogap Array

A nanogap array with centimeter size (1.0 cm × 1.0 cm) was prepared using a through-hole AAO mask [34–36]. The primary step is the opposite oblique evaporation of Ag 2 times, as shown in Fig. 1(a), and the detailed process can be found in the experimental section. Figure 1(b) shows the morphology of the AAO we used. The cross section of the AAO is a vertical channel array structure. The period, aperture size, and thickness of the AAO template are 125, 100, and 430 nm, respectively. Figure 1(c) shows the SEM images of the nanogap array.

An ordered nanogap array can be observed, and each nanogap is composed of two semiellipsoids with long axis diameters and short axis diameters of 74 and 46 nm, respectively. The height of the two Ag semiellipsoids is 30 and 39 nm. The distance between gaps is optimized by changing the tilt angle of the stage and the thickness of the evaporated Ag. The gap distance in each nanogap unit we can achieve in our experimental condition is approximately 8 nm, as shown in Fig. 1(d).

B. Plasmon of the Ag Nanogap Array

SERS is a plasmon-based optical phenomenon, and the SERS intensity is proportional to the fourth square of the local EM field [38]. Thus, SERS is an ideal way to indicate the local EM field intensity. Since the Ag nanogap is anisotropic, excitations of two polarization directions were adopted, as presented in Fig. 2(a), in which the projection of the polarization direction of the incident light in the nanogap plane is perpendicular (⊥) or parallel (//) to the nanogap axis. The TE-polarized incident light (the polarization direction is perpendicular to the incident plane) illuminates directly on the nanogap array with an incident angle (θ_1) ranging from 35° to 75°, and the reflectance spectra are collected from corresponding reflection direction, while the collection angle (θ_2) for SERS signals was steady at 60°. Figure 2(b) shows the reflectance spectra of the Ag nanogap array on a silica slide. It can be found that a broad dip is observed both in the cases of ⊥ or //. Figures 2(c) and 2(d) display the corresponding SERS spectra recorded at different incident angles, in which the strongest SERS signals appear at the resonance angles marked as the dashed lines ($\theta_1 = 65°$ for ⊥ and $\theta_1 = 51°$ for //). The intensity of SERS under the resonance angle of the case // is much stronger than that of the case ⊥, as shown in Fig. 2(e), which proves this nanogap array is polarization-dependent.

C. Plasmon of the Ag Nanogap Array with the WG

With respect to the direct excitation way, as described above, a WG structure is adopted to boost the nanogap array. The WG can capture the incident light and cause the extreme attenuation of the reflected light recorded from the prism side, which generates an enhanced EM field of an order of magnitude on the surface of the WG under the leaky WG modes [26]. Thus, the local EM field at gaps of the nanogap array is expected to be enhanced by coupling with the WG mode. Figure 3(a) shows the schematic diagram and SEM image of the WG used in this work, including a 35 nm Ag/600 nm SiO_2/air three-layered configuration, which is the same as in our previous study [28].

Coupling the incident light into a planar WG to form the WG mode usually needs an optical coupler, such as a prism or a large NA lens [32,33,39]. Figure 3(b) shows a prism as a light coupler for the WG, the measured reflectance spectra under TE and TM (the polarization direction is perpendicular or parallel to the incident plane) both give several narrow dips, indicating resonant modes. But no dips are observed in the reflectance spectra of a WG when directly excited from the air side, as shown in Fig. 3(c), indicating that the resonance conditions of the WG are unmatched.

Traditional optical couplers are not applied in this work. As shown in Fig. 4(a), the incident light is directly irradiated on the nanogap array from the air side to allow the plasmon resonance to first launch. Interestingly, we observed different reflectance spectra compared to the WG without nanogap array and significantly enhanced SERS spectra compared to the nanogap array without a WG. The WG modes are identified by the reflectance spectra under TE and TM polarizations to obtain the best coupling angle between the incident light and the nanogap array with the WG, noted as *TE – ⊥, *TE–//, *TM – ⊥, and *TM–//. Figure 4(b) shows the reflectance spectra for the four cases. They all display broad dips, with obvious attenuation of reflected light. Considering there are no dips in the reflectance spectra of the WG, as shown in Fig. 3(c), the similar broad dips in the reflectance spectra of nanogap array without a WG, as shown in Fig. 2(b), and the broad plasmon band of the Ag nanogap array as shown in Fig. 4(c), we suspect the broadening of the dips is caused by the absorption of the nanogap array. Figure 4(d) shows the corresponding SERS performance; the SERS intensity shows great enhancement. It can be observed that the SERS intensities of two // cases are much stronger than those of the ⊥ cases ($I_{*\mathrm{TE}-//} > I_{*\mathrm{TE}-\perp}$, $I_{*\mathrm{TM}-//} > I_{*\mathrm{TM}-\perp}$), which is consistent with the nanogap array without a WG, as presented in Fig. 2(e). The lowest detection concentration is 1.0×10^{-13} mol/L, as shown in Fig. 4(e).

Meanwhile, the use of a prism as an optical coupler has also been studied in detail; the enhancements of the same order of magnitude can be observed, as shown in Fig. 5. The incident light and the collected reflectance spectra are from the prism

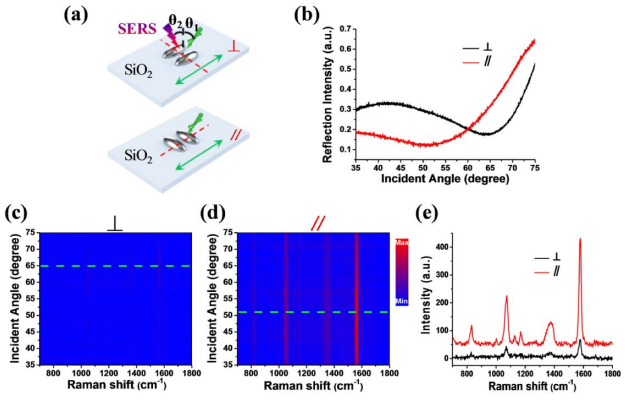

Fig. 2. (a) Schematic diagram of the polarization direction and nanogap axis; (b) reflectance spectra of the nanogap array in the cases of ⊥ and //; (c) and (d) SERS profiles of 4-MBA at different incident angles in the cases of ⊥ and //; (e) SERS spectra of 4-MBA on the nanogap array above a silica slide under the resonance angles [65° for case ⊥ and 51° for case //, along dashed lines in (c) and (d)].

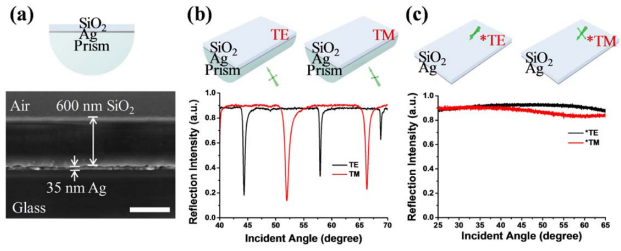

Fig. 3. (a) Schematic diagram and SEM image of the WG; the scale bar is 500 nm. (b) and (c) The measured reflectance spectra of the WG without nanogap array from the prism side and from the air side.

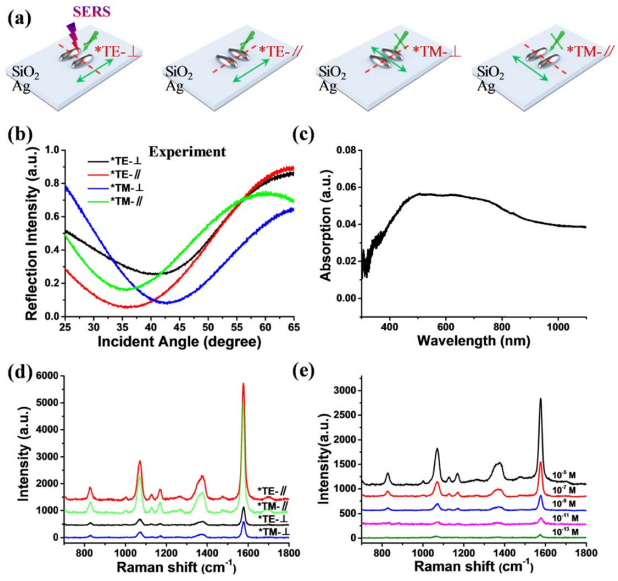

Fig. 4. (a) Schematic diagram of the polarization direction and nanogap axis; (b) measured reflectance spectra of the nanogap array with the WG excited from the air side for the four cases; (c) absorption spectrum of the Ag nanogap array with 8 nm gaps; (d) SERS spectra of a 4-MBA ethanol solution for the four cases; (e) SERS spectra of 4-MBA at different concentrations obtained on Ag nanogap array with the WG in the *TE−// cases.

side, and the objective lens for collecting SERS signals is vertical to the WG on the air side all through the detections. The four cases, as shown in Fig. 5(a) (TE − ⊥, TE−//, TM − ⊥, and TM−//) are tested, and Fig. 5(b) shows the reflectance spectra of the nanogap array with the WG in the four cases. The dips in reflectance spectra can be observed, which indicate the incident light couples with the nanogap array with the WG to an extreme. Figure 5(c) shows the corresponding SERS performance. It can be observed that the SERS intensities of two // cases are much stronger than those of the ⊥ cases ($I_{TE-//} > I_{TE-\perp}$, $I_{TM-//} > I_{TM-\perp}$). Furthermore, TM modes capture more incident light and provide stronger SERS signals than TE modes ($I_{TM-//} > I_{TE-//}$, $I_{TM-\perp} > I_{TE-\perp}$). To further investigate the local EM field, FDTD simulation is also carried out to simulate the reflectance spectra and the EM field distributions of the nanogap array, with the WG excited from the prism side. Figure 5(d) shows that dips exist for the four cases, and the variation trends of the resonance angles and the depths are consistent with the experimental results. Deviations between the simulation and experiment might be caused by the imperfect structure and the small change of the refractive index because of the assembled probe molecules. Figure 5(e) shows the corresponding EM field distributions and proves again the local EM fields of two // cases are much stronger than those of the ⊥ cases ($I_{TE-//} > I_{TE-\perp}$, $I_{TM-//} > I_{TM-\perp}$), and TM modes provide a stronger EM field than the TE modes ($I_{TM-//} > I_{TE-//}$, $I_{TM-\perp} > I_{TE-\perp}$).

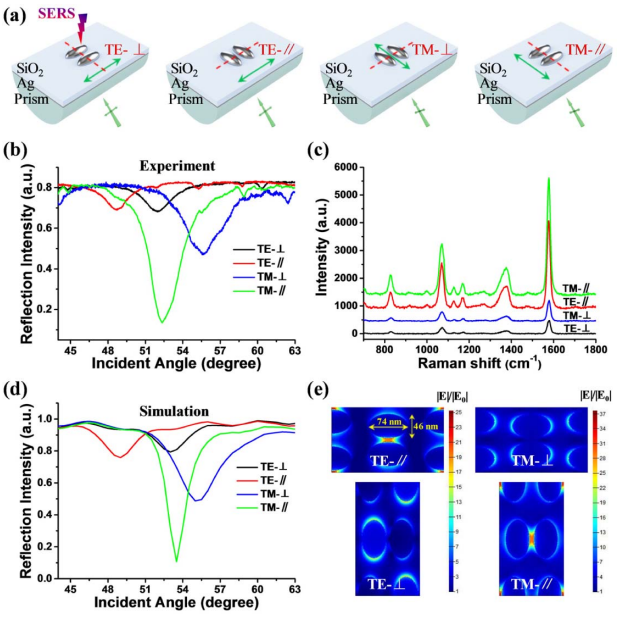

Fig. 5. (a) Schematic diagram of the polarization direction and nanogap axis for the four cases; (b) measured reflectance spectra of the nanogap array with the WG excited from the prism side for the four cases; (c) SERS spectra of a 4-MBA ethanol solution for the four cases; (d) and (e) simulated reflectance spectra and EM field distribution for the four cases, respectively.

Figures 6(a) and 6(b) show the dark-field images of the nanogap array without and with the WG, which can more intuitively display the EM field enhancement brought by the WG structure. Significantly, a brighter image is provided by the WG. The incident angle is calculated as 53.1° based on the NA of the lens. Although it is not the optimized incident angle, the integral intensity is improved approximately 2.2 times by the WG excited and collected from the air side, as shown in Fig. 6(c). Together with the SERS signals, dark-field imaging also performs the EM field enhancement by the WG without optical couplers.

D. Physical Mechanism of the Plasmon/WG Near-Field Coupling

FDTD simulation was applied for a deeper understanding of the EM field enhancement by the WG without optical couplers. Figures 7(a) and 7(b) show the simulated reflectance spectra and corresponding EM distributions of the nanogap array with WG coupling, as presented in Fig. 4(a). All four cases show broad dips in the reflectance spectra, which agree with the experimental results as shown in Fig. 4(b). Under the light irradiation, a part of the EM fields at the gap diffuse into the WG layer at the air/SiO_2 interface. Moreover, the alternately enhanced EM fields in the WG layers are also identifiable, as shown in Fig. 7(b), which indicates the WG modes form under

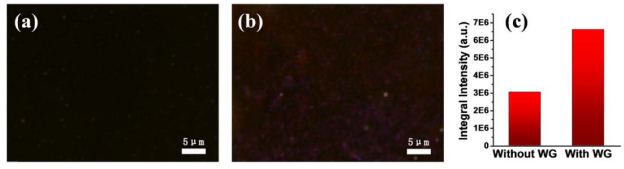

Fig. 6. Dark-field images of nanogap array (a) on a silica slide without a WG and (b) on a WG; (c) integral intensity of dark-field images.

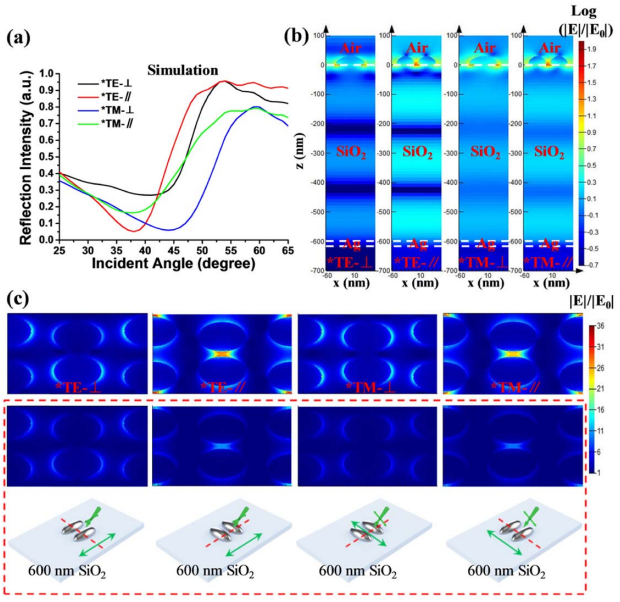

Fig. 7. (a) Simulated reflectance spectra for the four cases; (b) simulated EM field distributions for the four cases; (c) comparison of the EM field distributions of the nanogap array with the WG (top row, with 600 nm SiO_2 film and 35 nm Ag film) and without the WG (middle row, with only 600 nm SiO_2 film) for the four cases.

the light coupler of the nanogap array. Considering the Maxwell's equations, it is the standing wave in the SiO_2 layer. Because of the continuity of wave function at the boundary, the enhanced EM field near the WG/air interface in the WG layer causes an enhanced evanescent field on the surface of the WG [28]. As shown in Fig. 7(c), the EM fields of the nanogap arrays with the WG for the four cases are significantly stronger than that for a nanogap array on a 600 nm SiO_2 film. Therefore, the physical process of the nanogap array can be inferred. First, the incident light excites the LSPR of the nanogap array. Subsequently, the LSPR diffuses into the WG layer and interacts with the WG mode through the near-field coupling. As a result, the evanescent field on the surface of the WG further enhances the EM field of the nanogap array.

It is worth noting that the transmitted light through the nanogap array will also be reflected by the Ag film of the WG, and the reflected light excites the LSPR of the nanogap again. However, we cannot isolate the contribution of the reflection of the Ag film from the WG resonance modes because it has been involved in the WG part as a reflection mirror. Usually, the reflection effect can bring high reflectivity in the reflection spectra. But no obviously increased reflectivity is observed by comparing the red curves or the black curves in Figs. 2(b) and 4(b), and there is even decreased reflectivity for the *TE–// case after adding the Ag film. From Fig. 7(b), we also observe the WG resonance has been most improved in the case of *TE–//. Thus, the WG mode, rather than the reflection of the Ag film, plays the main role in the EM field enhancement.

Although the EM field of the nanogap array with the WG can also be enhanced through prism excitation, it is a completely opposite physical process, in which the WG resonance is first excited to come up multiple total internal reflections on the upper and lower interfaces of a WG layer, forming WG leaky modes [28]. Then, the plasmon of the nanogap array was excited and coupled through the leaky modes of the WG.

E. Comparison

The SERS intensities of the nanogap array without the WG (⊥ and //), with the WG excited by prism coupling (TE – ⊥ to TM–//), and with the WG excited by near-field coupling (*TE – ⊥ to *TM–//) are compared in Fig. 8. The nanogap arrays with the WG excited by near-field coupling at *TE–// provides the best SERS enhancement. Meanwhile, the nanogap array with the WG excited from the prism side at TM–// and the air side at *TM–// are only slightly weaker than at *TE–//. The strongest SERS intensity (*TE–//) is enhanced by 11 times relative to the nanogap array without the WG (//), indicating the local EM field can be improved approximately 1.8 times by the WG coupling experimentally ($\sqrt[4]{11} \approx 1.8$), which is slightly lower than the predicted results by FDTD, which creates 2.2 times stronger EM field in theory. To quantify the enhancement capability, the EM fields of the Ag nanogap array with gradually decreasing gaps (without the WG) are simulated. The hotspot area starts shrinking and is localized at the gap region with the decreasing gap distance, as shown in Fig. 9(a), and as disclosed in previous publications [40]. The strongest EM field intensity is dramatically improved, as shown in Fig. 9(c). We further calculated the integral intensity of the EM field, which was 10 times higher than at a hotspot region, as shown in Fig. 9(d). Although the hotspot becomes localized, the overall gain of the EM still increases, while the gap distance reduces. As we discussed above, 1.8 times the EM field amplification is provided by the plasmon/WG coupling mode. According to the integral intensity in Fig. 9(d), a 5 nm gap nanogap array without a WG can offer 1.8 times the comparable EM field relative to the 8 nm nanogap array without the WG. In other words, the 8 nm gap with the WG achieves an equivalent EM field to the 5 nm gap without the WG. The EM field distribution of an 8 nm gap nanogap array with the WG is also shown in Fig. 9(b), presenting a much larger hot area than the 5 nm nanodimer array without the WG.

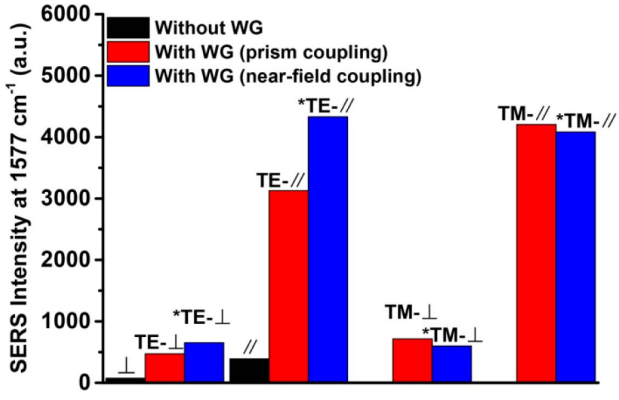

Fig. 8. Comparisons of the SERS intensities of the nanogap array without the WG and with the WG, including the prism side excitation and the air side excitation.

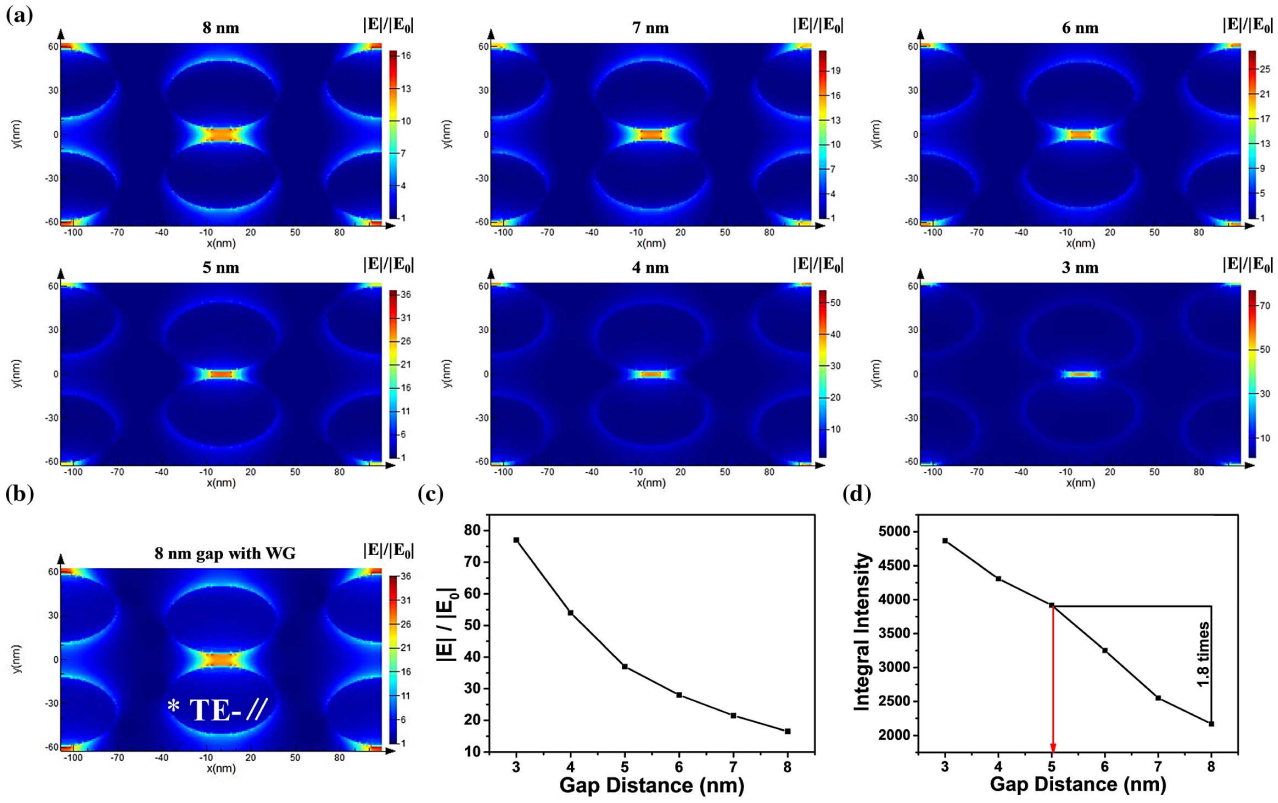

Fig. 9. (a) EM field distributions of the nanogap array without the WG at different gap distances, ranging from 8 to 3 nm; (b) EM field distribution of 8 nm gap nanogap array with the WG; (c) the strongest EM field at different gap distances, ranging from 8 to 3 nm; (d) integral intensity of the EM field (over 10 times) at different gap distances, ranging from 8 to 3 nm.

4. CONCLUSIONS

In summary, we demonstrated an optical WG/plasmon coupling way to boost a sub-10 nm gap plasmonic nanogap array. The WG mode can be excited through the near-field coupling of the nanogap array and then feed back to the nanogap array, achieving 1.8 times the EM field amplification in the gap regions. Although the plasmon-triggered WG resonance suffers from a weaker enhancement relative to our previous work, it may be optimized by changing the thicknesses of SiO_2 or wavelength of the incident light, which is also a direction of our future research. This strategy boosts the hotspots while maintaining the geometric size of gaps, thereby offering possible practical implementations for a wide range of hotspot-related applications, especially for plasmonic sensing and imaging.

Funding. National Natural Science Foundation of China (21573087, 21573092, 21603211, 21873039); Jilin Province Young Talent Fund Projects (20180520156JH).

Disclosures. The authors declare no conflicts of interest.

REFERENCES

1. Z. Liu, W. Hou, P. Pavaskar, M. Aykol, and S. B. Cronin, "Plasmon resonant enhancement of photocatalytic water splitting under visible illumination," Nano Lett. **11**, 1111–1116 (2011).
2. C. Y. Li, M. Meng, S. C. Huang, L. Li, S. R. Huang, S. Chen, L. Y. Meng, R. Panneerselvam, S. J. Zhang, B. Ren, Z. L. Yang, J. F. Li, and Z. Q. Tian, "'Smart' Ag nanostructures for plasmon-enhanced spectroscopies," J. Am. Chem. Soc. **137**, 13784–13787 (2015).
3. Z. Yin, Y. Wang, C. Song, L. Zheng, N. Ma, X. Liu, S. Li, L. Lin, M. Li, Y. Xu, W. Li, G. Hu, Z. Fang, and D. Ma, "Hybrid Au-Ag nanostructures for enhanced plasmon-driven catalytic selective hydrogenation through visible light irradiation and surface-enhanced Raman scattering," J. Am. Chem. Soc. **140**, 864–867 (2018).
4. A. A. Yanik, A. E. Cetin, M. Huang, A. Artar, S. H. Mousavi, A. Khanikaev, J. H. Connor, G. Shvets, and H. Altug, "Seeing protein monolayers with naked eye through plasmonic Fano resonances," Proc. Natl. Acad. Sci. USA **108**, 11784–11789 (2011).
5. R. Bhattacharya, C. Indukuri, N. Begam, O. H. Seeck, and J. K. Basu, "Plasmonic lipid bilayer membranes for enhanced detection sensitivity of biolabeling fluorophores," Adv. Funct. Mater. **25**, 7233–7242 (2015).
6. Y.-T. Chen, Y.-Y. Liao, C.-C. Chen, H.-H. Hsiao, and J.-J. Huang, "Surface plasmons coupled two-dimensional photonic crystal biosensors for Epstein-Barr virus protein detection," Sens. Actuators B Chem. **291**, 81–88 (2019).
7. M. H. Tahersima, M. D. Birowosuto, Z. Ma, W. C. Coley, M. D. Valentin, S. Naghibi Alvillar, I. H. Lu, Y. Zhou, I. Sarpkaya, A. Martinez, I. Liao, B. N. Davis, J. Martinez, D. Martinez-Ta, A. Guan, A. E. Nguyen, K. Liu, C. Soci, E. Reed, L. Bartels, and V. J. Sorger, "Testbeds for transition metal dichalcogenide photonics: efficacy of light emission enhancement in monomer vs dimer nanoscale antennae," ACS Photon. **4**, 1713–1721 (2017).
8. M. G. Lee, S. Yoo, T. Kim, and Q. H. Park, "Large-area plasmon enhanced two-dimensional MoS_2," Nanoscale **9**, 16244–16248 (2017).
9. Z. Q. Wu, J. L. Yang, N. K. Manjunath, Y. J. Zhang, S. R. Feng, Y. H. Lu, J. H. Wu, W. W. Zhao, C. Y. Qiu, J. F. Li, and S. S. Lin, "Gap-mode surface-plasmon-enhanced photoluminescence and photoresponse of MoS_2," Adv. Mater. **30**, 1706527 (2018).

10. S. Nie and S. R. Emory, "Probing single molecules and single nanoparticles by surface-enhanced Raman scattering," Science **275**, 1102–1106 (1997).
11. X. Chen, C. Ciraci, D. R. Smith, and S. H. Oh, "Nanogap-enhanced infrared spectroscopy with template-stripped wafer-scale arrays of buried plasmonic cavities," Nano Lett. **15**, 107–113 (2015).
12. T. Zhang, Y. Sun, L. Hang, H. Li, G. Liu, X. Zhang, X. Lyu, W. Cai, and Y. Li, "Periodic porous alloyed Au-Ag nanosphere arrays and their highly sensitive SERS performance with good reproducibility and high density of hotspots," ACS Appl. Mater. Interfaces **10**, 9792–9801 (2018).
13. D. K. Lim, K. S. Jeon, J. H. Hwang, H. Kim, S. Kwon, Y. D. Suh, and J. M. Nam, "Highly uniform and reproducible surface-enhanced Raman scattering from DNA-tailorable nanoparticles with 1-nm interior gap," Nat. Nanotechnol. **6**, 452–460 (2011).
14. C. Chi, F. Vargas-Lara, A. V. Tkachenko, F. W. Starr, and O. Gang, "Internal structure of nanoparticle dimers linked by DNA," Acs Nano **6**, 6793–6802 (2012).
15. S. A. Belhout, F. R. Baptista, S. J. Devereux, A. W. Parker, A. D. Ward, and S. J. Quinn, "Preparation of polymer gold nanoparticle composites with tunable plasmon coupling and their application as SERS substrates," Nanoscale **11**, 19884–19894 (2019).
16. H. Duan, A. I. Fernandez-Dominguez, M. Bosman, S. A. Maier, and J. K. Yang, "Nanoplasmonics: classical down to the nanometer scale," Nano Lett. **12**, 1683–1689 (2012).
17. A. D. Mueller, L. Y. M. Tobing, and D. H. Zhang, "Combining sonicated cold development and pulsed electrodeposition for high aspect ratio sub-10 nm gap gold dimers for sensing applications in the visible spectrum," Nanoscale **10**, 5221–5228 (2018).
18. E. Menumerov, S. D. Golze, R. A. Hughes, and S. Neretina, "Arrays of highly complex noble metal nanostructures using nanoimprint lithography in combination with liquid-phase epitaxy," Nanoscale **10**, 18186–18194 (2018).
19. X. Li, Y. Zhang, Z. X. Shen, and H. J. Fan, "Highly ordered arrays of particle-in-bowl plasmonic nanostructures for surface-enhanced Raman scattering," Small **8**, 2548–2554 (2012).
20. F. Laible, D. A. Gollmer, S. Dickreuter, D. P. Kern, and M. Fleischer, "Continuous reversible tuning of the gap size and plasmonic coupling of bow tie nanoantennas on flexible substrates," Nanoscale **10**, 14915–14922 (2018).
21. E. J. Zeman and G. C. Schatz, "An accurate electromagnetic theory study of surface enhancement factors for Ag, Au, Cu, Li, Na, Al, Ga, In, Zn, and Cd," J. Phys. Chem. **91**, 634–643 (1987).
22. C. Sonnichsen, T. Franzl, T. Wilk, G. von Plessen, J. Feldmann, O. Wilson, and P. Mulvaney, "Drastic reduction of plasmon damping in gold nanorods," Phys. Rev. Lett. **88**, 077402 (2002).
23. A. Shalabney, J. George, H. Hiura, J. A. Hutchison, C. Genet, P. Hellwig, and T. W. Ebbesen, "Enhanced Raman scattering from vibro-polariton hybrid states," Angew. Chem. Int. Ed. **54**, 7971–7975 (2015).
24. J. del Pino, J. Feist, and F. J. Garcia-Vidal, "Signatures of vibrational strong coupling in Raman scattering," J. Phys. Chem. C **119**, 29132–29137 (2015).
25. Y. J. Gu, S. P. Xu, H. B. Li, S. Y. Wang, M. Cong, J. R. Lombardi, and W. Q. Xu, "Waveguide-enhanced surface plasmons for ultrasensitive SERS detection," J. Phys. Chem. Lett. **4**, 3153–3157 (2013).
26. S. Wang, Z. Wu, L. Chen, Y. Gu, H. Wang, S. Xu, and W. Xu, "Leaky mode resonance of polyimide waveguide couples metal plasmon resonance for surface-enhanced Raman scattering," J. Phys. Chem. C **119**, 24942–24949 (2015).
27. H. L. Wang, Y. Y. Wang, Y. Wang, W. Q. Xu, and S. P. Xu, "Modulation of hot regions in waveguide-based evanescent-field-coupled localized surface plasmons for plasmon-enhanced spectroscopy," Photon. Res. **5**, 527–535 (2017).
28. Y. Tian, H. Wang, W. Xu, Y. Liu, and S. Xu, "Waveguide-coupled localized surface plasmon resonance for surface-enhanced Raman scattering: antenna array as emitters," Sens. Actuators B Chem. **280**, 144–150 (2019).
29. Z. Wang, W. Guo, L. Li, B. Luk'yanchuk, A. Khan, Z. Liu, Z. Chen, and M. Hong, "Optical virtual imaging at 50 nm lateral resolution with a white-light nanoscope," Nat. Commun. **2**, 218 (2011).
30. Y. Yan, C. Xing, Y. Jia, Y. Zeng, Y. Zhao, and Y. Jiang, "Self-assembled dielectric microsphere array enhanced Raman scattering for large-area and ultra-long working distance confocal detection," Opt. Express **23**, 25854–25865 (2015).
31. L. Yang, Y. Yan, Q. Wang, Y. Zeng, F. Liu, L. Li, Y. Zhao, and Y. Jiang, "Sandwich-structure-modulated photoluminescence enhancement of wide bandgap semiconductors capping with dielectric microsphere arrays," Opt. Express **25**, 6000–6014 (2017).
32. D. B. Hu and Z. M. Qi, "Refractive-index-enhanced Raman spectroscopy and absorptiometry of ultrathin film overlaid on an optical waveguide," J. Phys. Chem. C **117**, 16175–16181 (2013).
33. X. M. Wan, D. F. Lu, R. Gao, J. Cheng, and Z. M. Qi, "Metal-clad waveguide resonance sensor using a mesoporous TiO_2 thin film as the chemical sensitive core layer," J. Phys. Chem. C **121**, 19173–19181 (2017).
34. H. Masuda, K. Yasui, and K. Nishio, "Fabrication of ordered arrays of multiple nanodots using anodic porous alumina as an evaporation mask," Adv. Mater. **12**, 1031–1033 (2000).
35. M. Frederiksen and D. S. Sutherland, "Direct modification of colloidal hole-masks for locally ordered hetero-assemblies of nanostructures over large areas," Nanoscale **6**, 731–735 (2014).
36. Q. Hao, H. Huang, X. Fan, Y. Yin, J. Wang, W. Li, T. Qiu, L. Ma, P. K. Chu, and O. G. Schmidt, "Controlled patterning of plasmonic dimers by using an ultrathin nanoporous alumina membrane as a shadow mask," ACS Appl. Mater. Interfaces **9**, 36199–36205 (2017).
37. Y. Liu, S. Xu, B. Tang, Y. Wang, J. Zhou, X. Zheng, B. Zhao, and W. Xu, "Note: Simultaneous measurement of surface plasmon resonance and surface-enhanced Raman scattering," Rev. Sci. Instrum. **81**, 036105 (2010).
38. S. Y. Ding, E. M. You, Z. Q. Tian, and M. Moskovits, "Electromagnetic theories of surface-enhanced Raman spectroscopy," Chem. Soc. Rev. **46**, 4042–4076 (2017).
39. B. Dong, W. Zhang, Z. Li, and M. Sun, "Remote excitation surface plasmon and consequent enhancement of surface-enhanced Raman scattering using evanescent wave propagating in quasi-one-dimensional MoO_3 ribbon dielectric waveguide," Plasmonics **6**, 189–193 (2010).
40. C. Y. Tsai, J. W. Lin, C. Y. Wu, P. T. Lin, T. W. Lu, and P. T. Lee, "Plasmonic coupling in gold nanoring dimers: observation of coupled bonding mode," Nano Lett. **12**, 1648–1654 (2012).

159.226.165.16 (北京 2021-04-12 02:14:56)